

DOI: 10.1002/

Article type: Full Paper

Determining the Optimized Interlayer Separation Distance in Vertical Stacked 2D WS₂:hBN:MoS₂ Heterostructures for Exciton Energy Transfer

*Wenshuo Xu, Daichi Kozawa, Yu Liu, Yuewen Sheng, Ke Wei, Volodymyr B. Koman, Shanshan Wang, Xiaochen Wang, Tian Jiang, Michael S. Strano, Jamie H. Warner**

Wenshuo Xu, Yuewen Sheng, Shanshan Wang, Xiaochen Wang, Prof. Jamie H. Warner
Department of Materials, University of Oxford, Parks Road, Oxford OX1 3PH, United Kingdom

E-mail: jamie.warner@materials.ox.ac.uk

Dr. Daichi Kozawa, Dr. Volodymyr B. Koman, Prof. Michael S. Strano
Department of Chemical Engineering, Massachusetts Institute of Technology, Cambridge, Massachusetts 02139, United States

Yu Liu, Ke Wei, Prof. Tian Jiang

College of Opto-Electronic Science and Engineering, National University of Defense Technology, Changsha 410073, China

Keywords: transition metal dichalcogenides, hexagonal boron nitride, 2D heterostructures, energy transfer, photoluminescence

Here, we use all chemical vapour deposition (CVD) grown materials to create VLH stacks of WS₂:hBN:MoS₂ with the thickness of hBN adjusted carefully from 0 to 16 layers to map out the optimal separation distances for PL enhancements and quenching. We show that (4±1) layers of hBN are the optimum for obtaining PL enhancement in our VLHs. Increasing thickness beyond this causes the enhancement factor to diminish, with the WS₂ and MoS₂ then behaving as isolated non-interacting monolayers. Femtosecond transient absorption spectroscopy confirms the energy transfer from MoS₂ to WS₂. The interlayer interactions studied by photoluminescence spectroscopy (PL) are highly sensitive to the input excitation power. For thin hBN separators (1-2 layers), the total PL emission switches from quenching to enhancement by increasing the laser power. The PL signal is further enhanced in cryogenic measurements due to the suppressed non-radiative decay channels. These results indicate how precise control over the spacing between MoS₂ and WS₂ layers using hBN can enable insights into energy transfer in the VLHs.

1. Introduction

The availability of more 2D materials than just graphene has allowed the expansion of application and science of 2D electronics and opto-electronics.^[1–9] In particular, monolayer transition metal dichalcogenides, such as WS₂ and MoS₂, have found widespread interest due to the direct band gap in the visible spectrum that emerges when they are monolayer.^[10–15] In bulk, these TMDs are indirect band gap materials and thus have quite different properties.^[10–12,16] Combining the metallic-like properties of graphene, the insulating behavior of hBN with the semiconducting properties of monolayer TMDs enables all 2D electronics and opto-electronics to be realized.^[2,3,17] These can be with either lateral geometry,^[2] or vertical stacked structures.^[3,17] The layer-by-layer assembly of 2D materials on top of each other builds complex vertical layered heterostructures (VLHs) that have unique properties through the strong interlayer interactions.^[18–29]

The VLHs have been used to produce new types of tunneling transistors, photodetectors and light emitting devices.^[3–7,27] In most of these cases, graphene is used as the metal electrode and monolayer TMDs as the active semiconductor material.^[3–5] The insertion of insulating hBN between the graphene and TMDs provides the tunnel barrier and tuning its thickness by layer number has shown to result in optimized field-effect mobility in VLHs.^[3] Without the hBN insulator between two TMDs, a type II heterojunction can be formed, such as in MoS₂:WS₂ bilayer stacks.^[19,26,29] In these systems the exciton is rapidly separated into the two layers, leading to quenching of the PL emission.^[20–24] Insights into the behavior of photoexcited excitons can be gained by photoluminescence spectroscopy and transient absorption (TA) spectroscopy of these VLHs.

Recent work has shown that the indirect recombination in WSe₂:MoS₂ heterobilayers could be suppressed by inserting dielectric hBN films in between.^[22] However, a systematic study on the number of hBN layers has yet to be performed and is important for determining

the optimized separation distance between two TMD layers for maximized energy transfer. For small separation distances, Dexter transfer is expected to dominate, which is associated with charge transfer and PL quenching. As the separation distance increases, Förster energy transfer can then arise, whereby dipole-dipole interactions lead to exciton transfer from one semiconductor to another.^[42] Finally as the separation distance further increases, interlayer interactions should diminish and the two semiconductors behave as isolated materials.^[30] Controlling the interlayer distance across this range of interactions in VLHs has yet to be investigated in detail.

The large exciton binding energy in WS₂ and MoS₂ promotes the study of many-body effects.^[31,32] Increasing the exciton generation rate with higher excitation power causes varied exciton density and in turn the relative population of excitons and trions in the material.^[32,33] The interlayer interactions between TMDs in VLHs should also be influenced by the excitation power, but to date there has been little investigation into this.

In this paper, we use CVD-grown WS₂, MoS₂ and hBN to create VLHs of WS₂:hBN:MoS₂ and MoS₂:hBN:WS₂ with tunable separation distance by adjusting the total number of hBN layers in between. We study the effects of input laser power as well as temperature on the PL properties of the VLHs. The WS₂ and MoS₂ are grown as isolated domains that enable their heterostructures to be easily identified by optical microscopy and also the measurement of PL from each monolayer and the heterostacked region can be conducted separately for a direct comparison of the PL signal magnitude. Similar to prior reports, the PL emission from WS₂ is significantly larger than MoS₂ and dominates the VLH emission.^[20,24] PL quenching or enhancement in VLHs can be evaluated by comparing the total integrated PL signal from the WS₂:hBN:MoS₂ region with that of the WS₂ monolayer. The influence of strain on the VLH interlayer interactions is probed by comparing two configurations, one where the WS₂ is as-grown with inbuilt strain and the MoS₂ is transferred

on top, and the other where the MoS₂ is as-grown with inbuilt strain and then the WS₂ is transferred on top. The presence of strain induces shifts in the band gap of TMDs, and alters the relative offsets in the band structure that generates the type II heterostructure interface.^[17,43,44] The CVD-grown materials permit large numbers of VLHs to be formed on a single 1 cm × 1 cm chip. Therefore multiple measurements can be provided to ensure the findings are consistent throughout the sample.

2. Results and Discussion

The constituent materials of the heterostructures, i.e., isolated WS₂ and MoS₂ domains and hBN continuous films, are synthesized via atmospheric pressure chemical vapour deposition (APCVD). To fabricate the vertical stacks, we used our recently reported sliding transfer method in isopropanol (IPA) to preserve the underlying TMD materials. The use of highly volatile solvent ensures no residues to be remained so that cleaner interfaces between the 2D layers can be generated compared to the conventional methods based on water.^[35] The cleanliness of interface is evidenced by the strong interlayer coupling of WS₂:MoS₂ (Figure S3 and Table S1, Supporting Information) and MoS₂:WS₂ (Figure S4 and Table S2, Supporting Information) heterostacks, as well as the annealing effects shown in Figure S16 (Supporting Information). Characterizations of the individual 2D materials to determine their structure and thickness involve scanning electron microscope (SEM), atomic force microscopy (AFM), and Raman spectroscopy (Figure S1 and S2, Supporting Information).

PL quenching has been previously observed in semiconducting heterostacks, for instance, TMD bilayers comprising a variety of materials, because the charge transfer process in the type II heterojunction can efficiently hinder the intrinsic excitonic recombination from either of the monolayers.^[20–24] We made reverse WS₂:MoS₂ and MoS₂:WS₂ heterobilayers and demonstrated this to be independent of the stacking sequence or excitation laser power (Figure S3 and S4, Table S1 and S2, Supporting Information). To change the interlayer

coupling behaviour, an insulating hBN barrier is inserted between the WS₂ and MoS₂ monolayers, shown schematically in **Figure 1a,b**. Figure 1c shows the optical microscope image of a VLH area where WS₂ and MoS₂ contain both regions that overlap and regions that do not. This allows the comparison between the isolated individual TMD layers and their stacks within the same domain. Figure 1d,e show the PL variations when utilizing monolayer hBN films, in terms of the integrated intensity and overall peak position, respectively, as a function of laser power. The quenching degree of the heterostacked regions gradually decreases with a red shift of the peak position as the input excitation power increases, indicative of suppressed interlayer charge transfer.^[20–22,25] For both the WS₂ and MoS₂ monolayers, higher excitation power produces more electrons and holes in the conduction bands and valence bands, respectively. The larger populations lead to increased Coulomb interactions between the WS₂ and MoS₂ monolayers through the electrons in the conduction bands and holes in the valence bands. Therefore the possibility is decreased of the electron transition from the conduction band of WS₂ to the conduction band of MoS₂, simultaneous with the reduced hole transition from the valence band of MoS₂ to the valence band of WS₂. The suppression of charge transfer results in decreased PL quenching under higher excitation power.

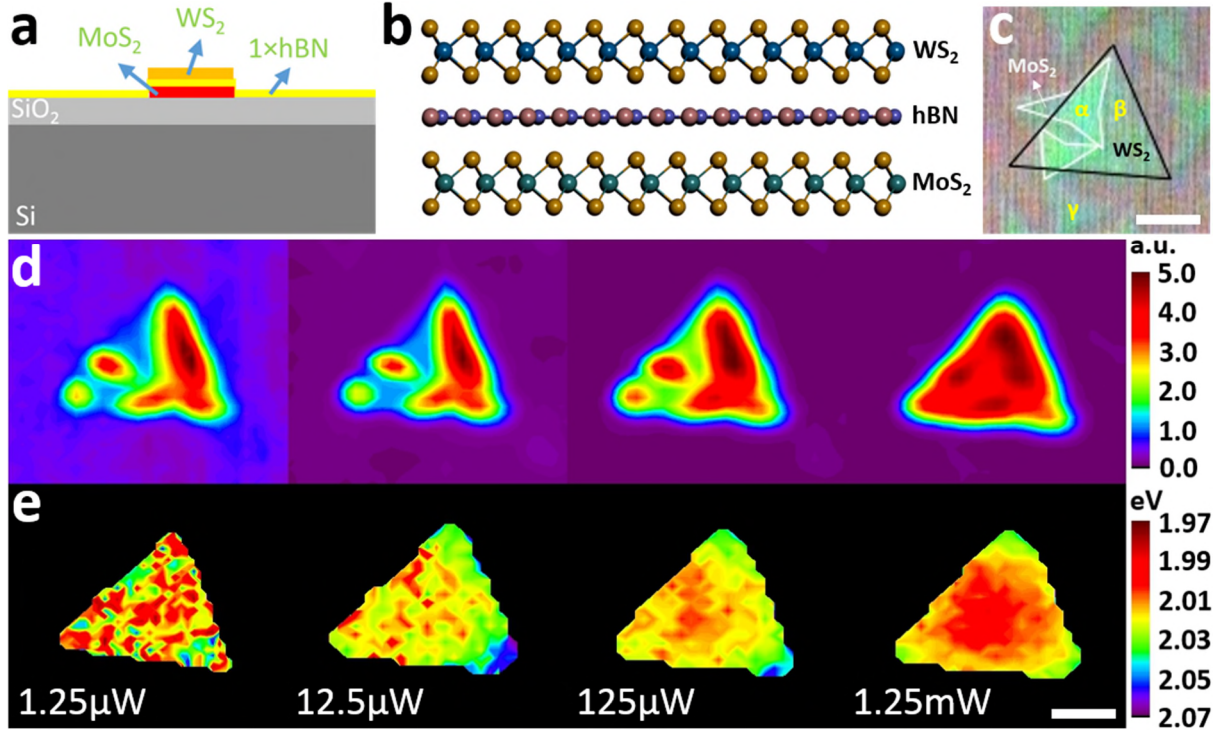


Figure 1. a) Schematic diagram, b) atomic model, and c) optical microscope image of the WS₂:1xhBN:MoS₂ VLH. Position α – WS₂:1xhBN:MoS₂, β – WS₂, and γ – MoS₂. 2D maps of d) normalized total integrated PL intensity of the VLH vs the WS₂ monolayer and e) overall PL peak position as a function of increasing excitation power (1.25 μ W, 12.5 μ W, 125 μ W, and 1.25 mW) across the region shown in (c). Scale bar: 10 μ m.

To understand the PL spectra from the WS₂:1xhBN:MoS₂ regions presented in Figure 1 in more detail, we used Gaussian fits to extract the relative contributions of excitons (A), trions (A⁻) and localized states (LS) to the total PL emission, as shown in **Figure 2**. We compare the two different excitation powers of 125 μ W and 1.25 mW for each TMD and their stacked configuration as these represent the two cases where the changes in charge/energy transfer are observed. For both the monolayers, the A peak arises from neutral exciton emission due to the direct transition at the K point, and the A⁻ peak is associated with the recombination of negatively charged excitons. In addition, the B peak of monolayer MoS₂ is located at a higher energy, which originates from another direct transition between the conduction and valence bands. The LS peak is normally related to structural disorders and/or impurities.^[32,34,40] The ratio of exciton/trion decreases for both the ‘pristine’ TMDs and the heterostructure. Figure 2a,d show that the total PL of the WS₂:1xhBN:MoS₂ stack is

primarily made up of the emission from WS₂, which is substantially stronger than that from MoS₂.

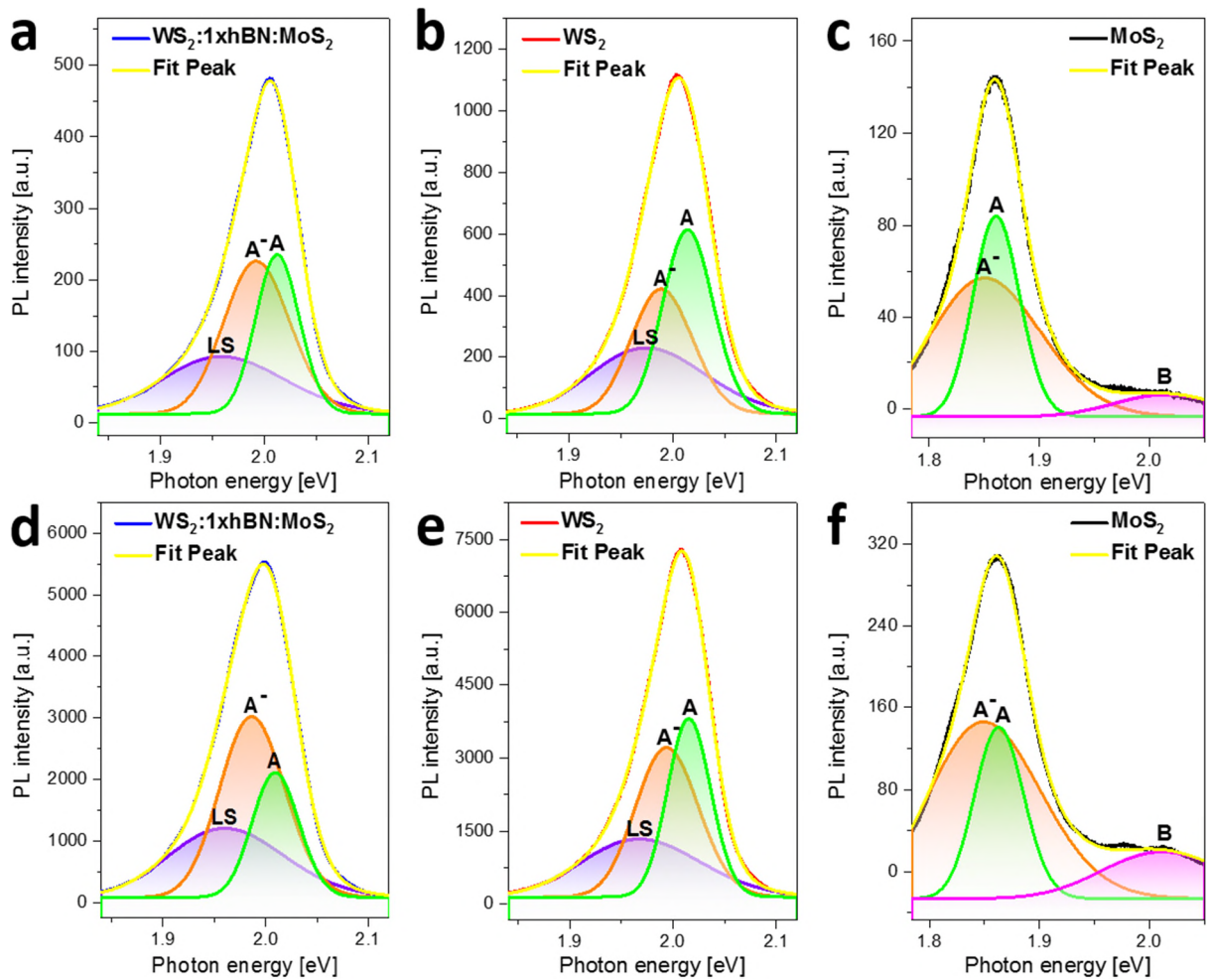


Figure 2. PL spectra of the positions marked as α , β , and γ in Figure 1c, with a–c) 125 μ W and d–f) 1.25 mW excitation powers. The total PL peaks are deconvoluted using Gaussian functions to extract exciton (A), trion (A[−]) and localized states (LS) emissions. The excitation power dependence of A, A[−], and LS is investigated in Figure S11 (Supporting Information).

Figure 3 shows the results when doubling the thickness of hBN to bilayer. The monolayer nature of WS₂ and MoS₂ domains are confirmed via Raman spectroscopy (Figure 3d),^[36,37] and the Raman modes of E' and A₁' from both the TMD layers are superpositioned in the heteroregions (Figure 3d). This suggests the combination of vibrational modes, which is also observed in the stacks without hBN spacer (Figure S3d, Supporting Information). The WS₂:2×hBN:MoS₂ region does not show quenching at higher excitation powers, but instead an enhanced PL intensity by a factor of 2.11 (Figure 3e). The total integrated PL intensity map in Figure 3f shows that the enhancement corresponds to the overlapping regions of WS₂

and MoS₂, and the PL peak position map, Figure 3g, indicates a blue shift in this VLH.

Another example is presented in Figure 3h and used to probe the PL dependence on the incident laser power. The PL maps in Figure 3i show that the PL signal of the stacked region switches from quenching at low excitation power (1.25 μ W) to enhancement at high excitation powers (12.5 μ W and above); furthermore, the enhancement degree increases with the excitation power. Similarly, the blue shift of the PL peak position becomes more evident at the increased laser power of 1.25 mW (Figure 3j). To prove the reversibility and rule out laser processing effects, we have cyclically excited the samples by inputting different laser powers alternatively (Figure S5, Supporting Information).

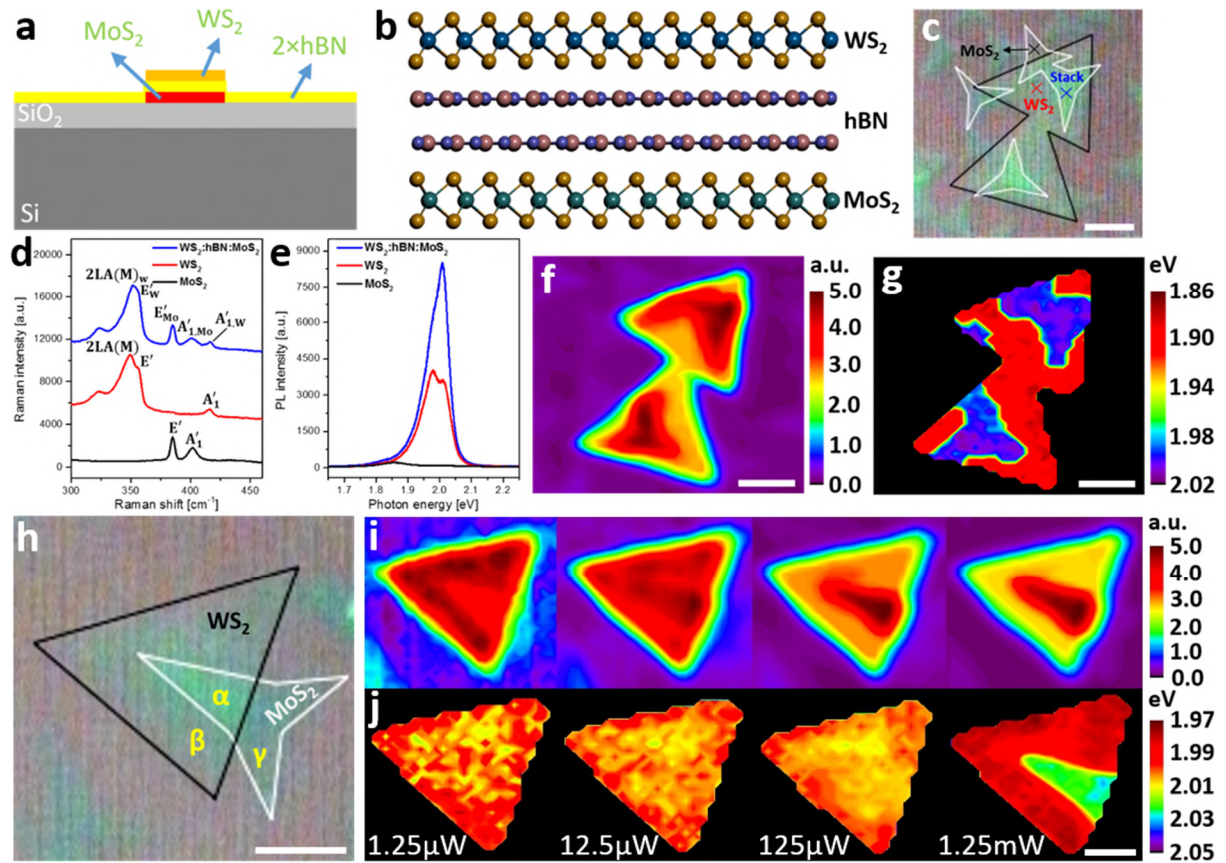


Figure 3. a) Schematic diagram, b) atomic model, and c) optical microscope image of a WS₂:2xhBN:MoS₂ VLH. d) Raman and e) PL spectra taken from the positions marked in (c). Raman – 12.5 mW excitation power and 3s acquisition time; PL – 125 μ W excitation power and 1s acquisition time. The subscript W represents WS₂, and Mo represents MoS₂. 2D maps of f) normalized total integrated PL intensity of the VLH vs the WS₂ monolayer and g) overall PL peak position across the region shown in (c). h) Optical microscope image of another WS₂:2xhBN:MoS₂ VLH (Position α – WS₂:2xhBN:MoS₂, β – WS₂, and γ – MoS₂), for which the 2D maps of normalized total integrated PL intensity of the VLH vs the WS₂

monolayer and overall PL peak position as a function of increasing excitation powers (1.25 μ W, 12.5 μ W, 125 μ W, and 1.25 mW) are shown in i) and j), respectively. Scale bar: 10 μ m.

Figure 4a–c and **d–f** show the Gaussian-fitted PL spectra for the VLH and the TMD monolayers at excitation powers of 125 μ W and 1.25 mW, respectively. The increase in laser power causes a more pronounced trion emission (i.e., a smaller exciton/trion ratio) for all the three regions. But the heterostack shows larger exciton/trion ratios relative to the WS₂ monolayer, especially under the higher excitation power of 1.25 mW (Figure 4a vs b and d vs e). This could be attributed to the injection of excitons from the MoS₂ to WS₂ monolayer via Förster energy transfer. As the PL quantum efficiency of the system is increased by the change in excitonic states,^[12,45] the enhanced signal in the VLH is even larger than the total intensity of the MoS₂ monolayer. However, the charge transfer is negligible in this VLH as the emission of interlayer exciton is highly suppressed by the hBN separator and the low yield has little contribution to the total PL signal. The varied exciton/trion ratios indicate a difference in the PL behaviour of these two systems and shed light on the origins of the PL enhancement that occurs under high input laser power. 2D maps of the exciton and trion peak positions at these two excitation powers, Figure 4g–j, show an increased blue shift for the trion emission with laser power, whereas little change is observed for the exciton emission.

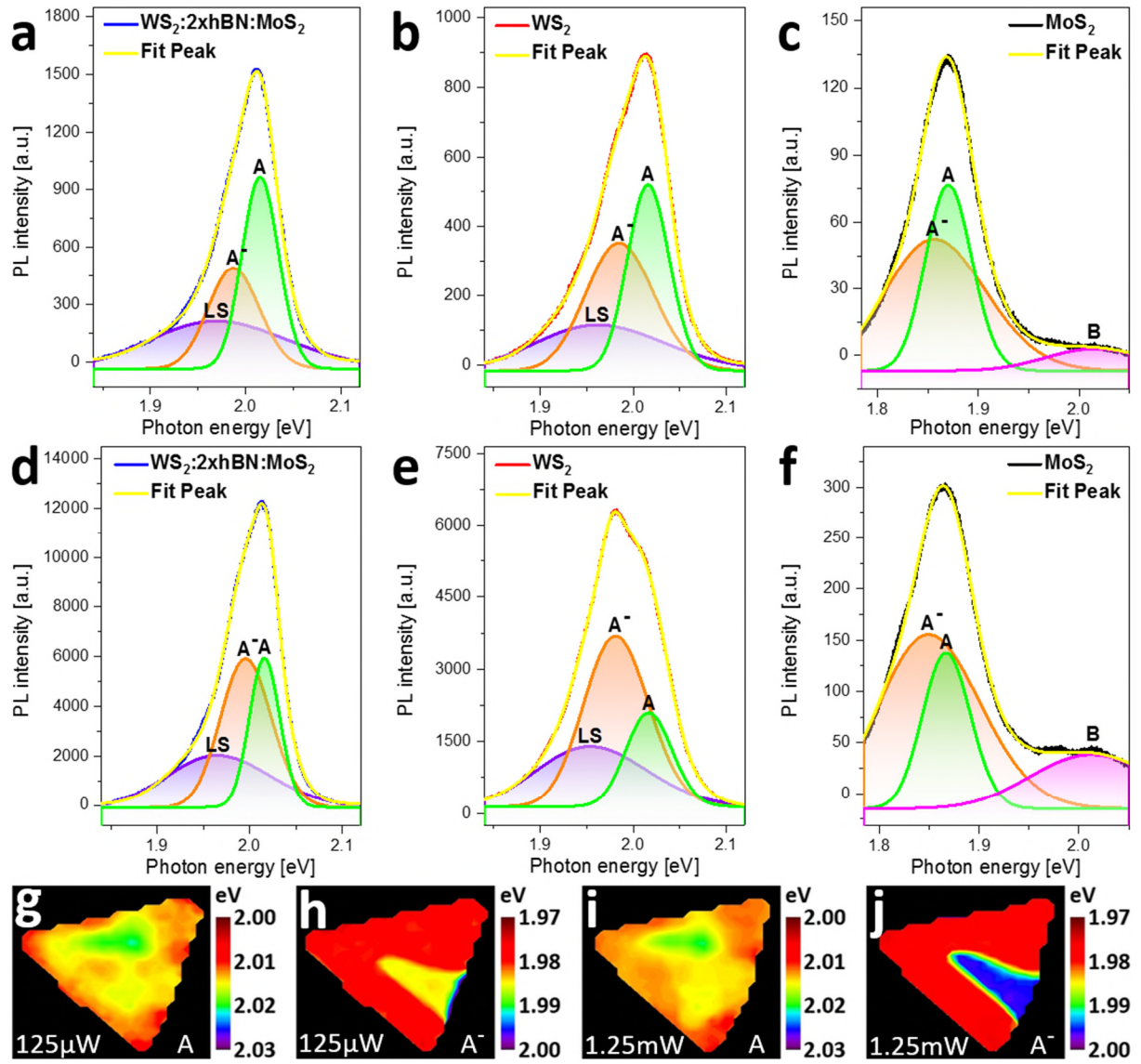


Figure 4. Gaussian-fitted PL spectra acquired by using a–c) 125 μW and d–f) 1.25 mW excitation powers for a,d) Position α ($\text{WS}_2:2\text{xhBN:MoS}_2$), b,e) Position β (WS_2), and c,f) Position γ (MoS_2), as marked in Figure 3h. g,i) Exciton and h,j) trion peak position maps for the sample region in Figure 3h under 125 μW and 1.25 mW excitation powers, respectively.

Further insights can be gained by reversing the stacking order and having WS_2 on the bottom and MoS_2 on the top, shown in **Figure 5**. In both cases, the bottom material was as-grown and this typically contains strain in the crystal lattice due to the CVD method. The presence of strain causes band gap modification, which will change the relative band offsets between WS_2 and MoS_2 monolayers and in turn the details of the type II heterostructure.^[17,43,44] Inbuilt strain can therefore lead to substantial PL red shift for monolayer WS_2 (Figure S6, Supporting Information).^[43] Figure 5 shows that though PL quenching is still observable in the reversed

stack of MoS₂:2×hBN:WS₂ under low excitation powers (1.25 μW and 12.5 μW), an enhancement of PL emerges while further increasing the laser excitation power. The exciton and trion peak positions at different laser powers are studied in Figure S7 (Supporting Information). Compared to the VLH with unstrained WS₂ (Figure 3 and 4), the VLH with strained WS₂ (Figure 5d–h) shows more quenching under low excitation powers; additionally, the increased LS emissions reveal that more structural disorders are involved because of the strain.^[40] However, at high laser power of 1.25 mW both stack configurations show the same level of PL enhancement (Figure 5o). The observation of this switching from PL quenching to enhancement in both VLHs indicates that it is not related to the local dielectric environment or exposure to air or damage, but is an intrinsic property that arises by overlapping WS₂ and MoS₂ with 2×hBN in between. Utilizing excitation power above 1.25 mW causes material degradation and this is the origin of the downturn in the PL ratio in Figure 5o.

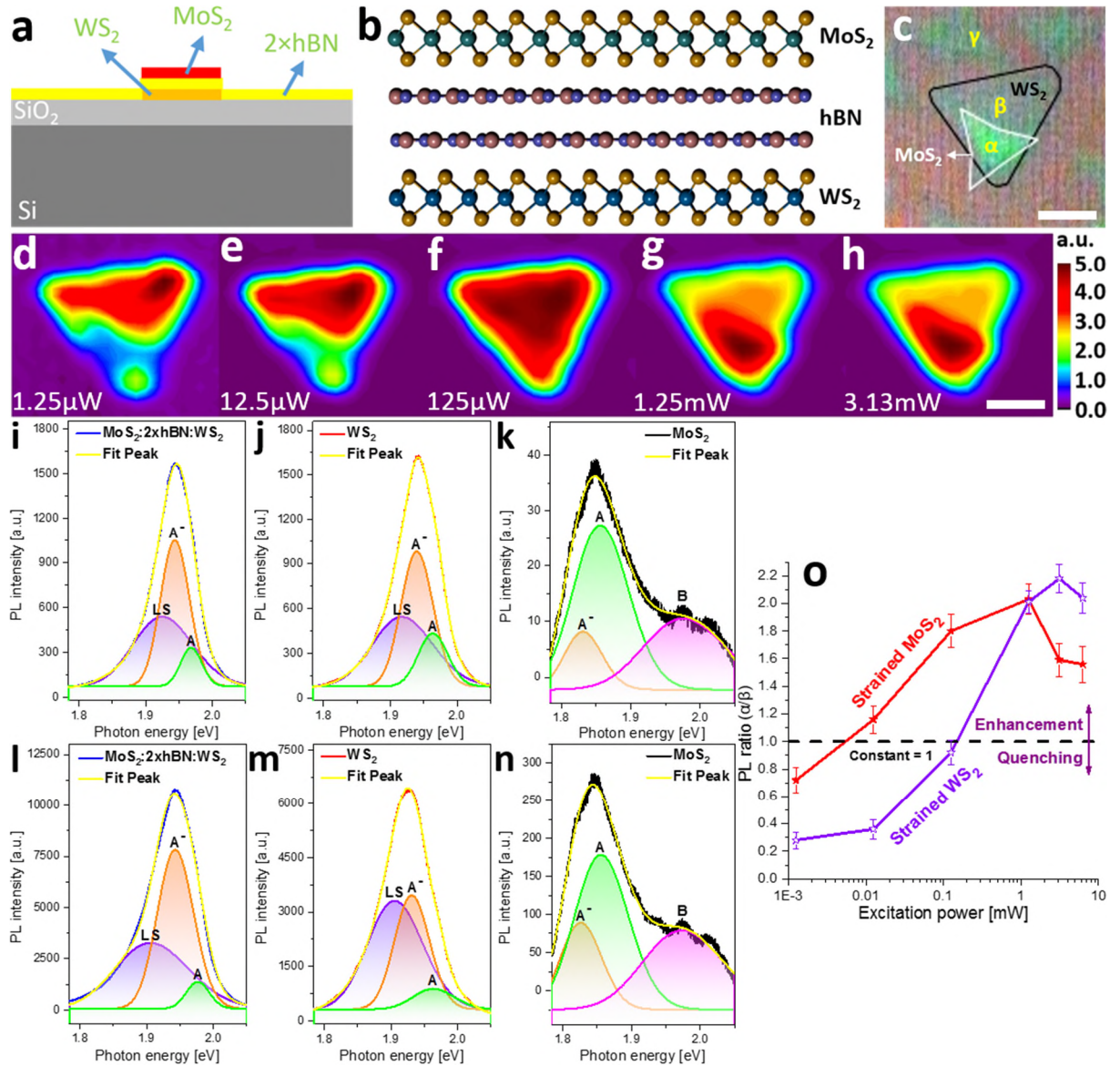


Figure 5. a) Schematic diagram, b) atomic model, and c) optical microscope image of the MoS₂:2xhBN:WS₂ VLH. d–h) 2D maps of normalized total integrated PL intensity of the VLH vs the WS₂ monolayer with increasing excitation powers (1.25 μW, 12.5 μW, 125 μW, 1.25 mW, and 3.13 mW) across the region shown in (c). Scale bar: 10 μm. Gaussian-fitted PL spectra acquired by using i–k) 125 μW and l–n) 1.25 mW excitation powers for i,l) Position α (MoS₂:2xhBN:WS₂), j,m) Position β (WS₂), and k,n) Position γ (MoS₂), as marked in (c). o) Plot of the PL ratio (total integrated PL intensity of Position α divided by that of Position β in the corresponding optical microscope image) as a function of input excitation power. Dashed line at PL ratio = 1 indicates the cross-over between PL quenching and enhancement. Each PL ratio in (o) is an averaged value with the error bar obtained on a statistical basis of 10 measurements.

The observation of PL quenching at low excitation powers in Figure 3, 4, and 5 for bilayer hBN spacers between WS₂ and MoS₂ indicates that charge transfer is still occurring and excitons are efficiently dissociated across the two TMD layers.^[19,20,26] However, the shift at high excitation powers to PL enhancement reveals that energy transfer becomes the dominant

mechanism in the VLH regions. Interlayer energy transfer is highly sensitive to distance and rapidly falls off as the separation increases. To explore this in more detail, **Figure 6** shows how the PL of the VLHs changes with increasing the hBN separator layer from 2, to 4 (Figure 6a–f), 6 (Figure 6g–l), 8 (Figure 6m–r), and 16 (Figure 6s–x), as a function of the input laser power. All these VLHs show PL enhancement under excitation powers of 125 μ W and above. However, increasing the hBN separator layers beyond 4 requires higher excitation power for observing enhanced PL signals due to the reduced strength of the interlayer interactions.

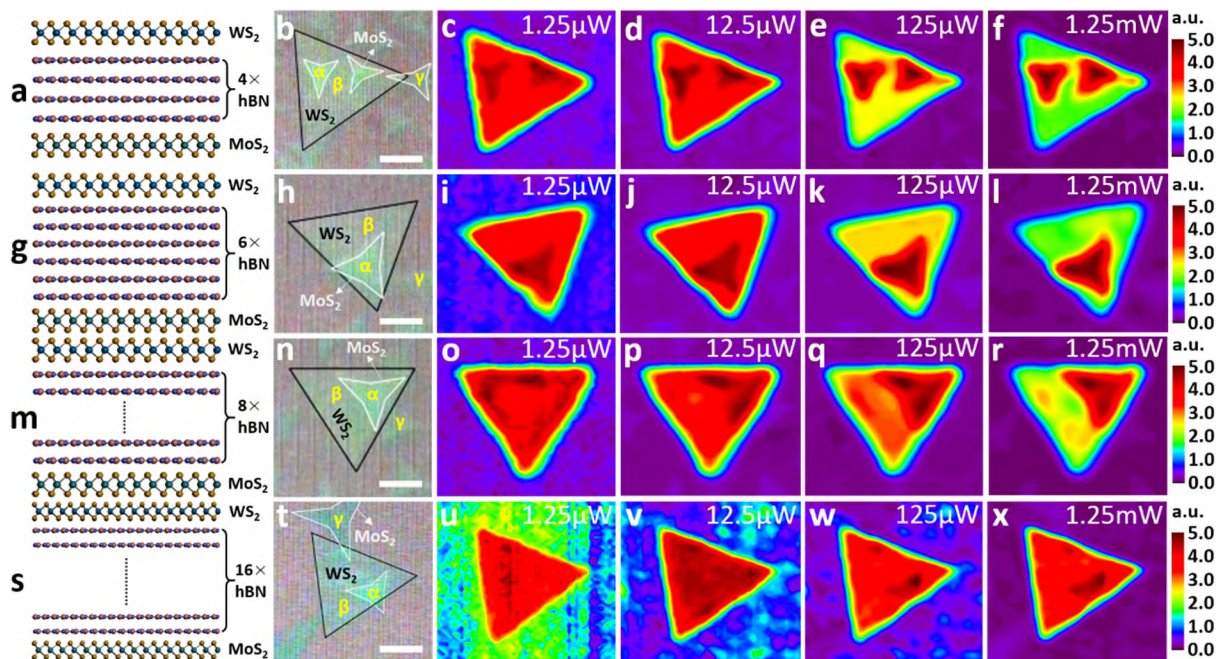


Figure 6. PL measurements on VLHs with increasing hBN separator thickness of a–f) 4 layers, g–l) 6 layers, m–r) 8 layers, and s–x) 16 layers. a,g,m,s) Atomic models of the VLH stack configurations. b,h,n,t) Optical microscope images of the respective heterostacks used in the mapping of normalized total integrated PL intensity of the VLH vs the WS₂ monolayer with increasing laser power for c–f) 4 layers, i–l) 6 layers, o–r) 8 layers, and u–x) 16 layers of hBN.

Figure 7a plots the PL ratio as a function of excitation power for all the hBN separator layers used in this study, including zero (no hBN involved). **Figure 7b** plots the PL ratio as a function of hBN layer number and suggests that (4 ± 1) layers are the optimal hBN thickness for PL enhancement. The dependence of separation distance allows the extrapolation to show that at a spacing of $\times 24$ hBN layers the two TMD layers are expected to act as isolated materials with negligible interactions. Since the degree of PL enhancement depends on the

incident excitation power, it is possible that ultrahigh input laser powers could be used to observe some effects even with $\times 24$ hBN layers, but it is more likely that the high-power laser would destroy the sample first. Detailed studies on the PL spectra are presented in Figure S8, S9, and S10 (Supporting Information). Considering both charge transfer and Förster energy transfer models enabled a fit to the experimental data for each excitation power (Figure 7b), using Equation 1. The fitting is elaborated and interpreted in Figure S12 and Table S3 (Supporting Information). The different distance dependences of charge transfer and Förster energy transfer lead to a peak in the PL ratio, similar to the experimental data. For short distances, energy transfer from WS₂ to MoS₂ dominates with a moderate fraction of charge transfer so that quenching occurs. As the distance then increases between the WS₂ and MoS₂ by adding more hBN layers, Förster energy transfer from MoS₂ to WS₂ overtakes charge transfer and the opposite energy transfer as the main interlayer interaction. The interesting aspect of this Förster energy transfer process is that the direction appears to be from the B exciton in MoS₂ to the A exciton state in WS₂, given the PL enhancement observed in WS₂ but not in MoS₂.

$$\frac{I}{I_0} = \left(1 + a_1 \frac{1}{1 + \left(\frac{R}{R_0} \right)^n} \right) \left(1 - a_2 - a_3 \exp\left(-\frac{2R}{a_B} \right) + a_4 \frac{1}{1 + \left(\frac{R}{R_0} \right)^n} \right) \quad (1)$$

, where R is the separation distance, $R_0 = 4.9$ nm is the Förster distance, $a_B = 1.53$ nm is the exciton Bohr radius which is referred to the previous reported value,^[41] a_1 and a_4 are the Förster energy transfer coefficients, a_2 is the non-radiative decay efficiency of excitons, a_3 is the charge transfer coefficient.

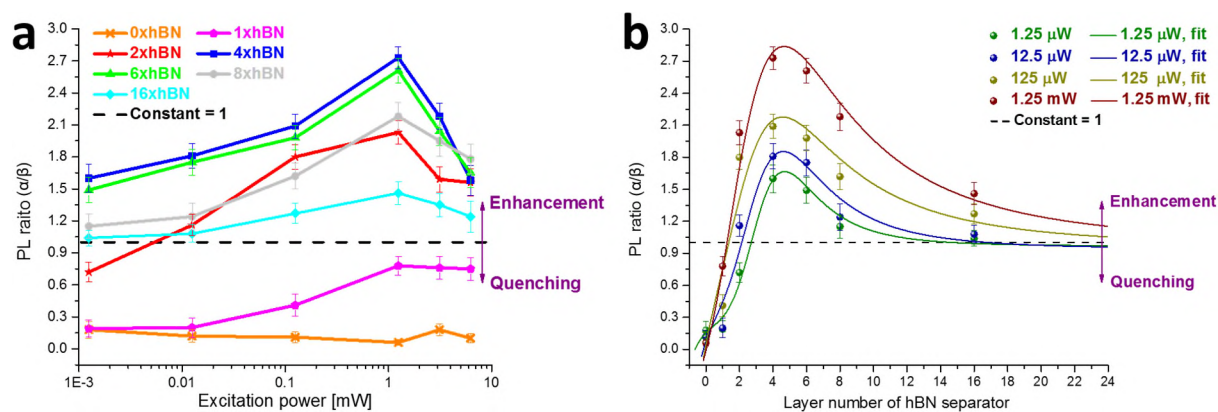


Figure 7. a) Plot of the PL ratio (total integrated PL intensity of Position α divided by that of Position β in the corresponding optical microscope image) as a function of input excitation power for different hBN separator layer numbers. b) Plot of the PL ratio as a function of hBN layer number in the VLHs under different excitation powers (solid lines – fit curves using Equation 1; dots – experimental data from panel (a)). Fitting parameters are listed in Table S3 (Supporting Information). Dashed line at PL ratio = 1 indicates the cross-over between PL quenching and enhancement. Each PL ratio is an averaged value with the error bar obtained on a statistical basis of 10 measurements.

We conducted femtosecond transient absorption spectroscopy to investigate the kinetics of the ultrafast photophysical interactions. Each region was excited by a ~ 120 fs pulse laser with an average energy of 300 nW. The results are shown in **Figure 8**, based on which the peak intensities and the associated photon energies are summarized in **Table 1**. The bleaching features correlate well with the photoinduced excitons, and the peak intensity reflects the density of the corresponding excitons. It is found that the bleaching signal caused by the emission of B excitons in MoS₂ monolayer is decreased (by $\sim 50\%$) in the stacked region, while those by WS₂ A and A⁻ are increased (by $\sim 78\%$ and 75% , respectively) compared to the WS₂ monolayer. These changes in light absorptions offer direct proof of the Förster energy transfer occurring from MoS₂ (B excitonic state) to WS₂ (A excitonic states) in the VLHs, which leads to the increase in quantum yield of the system and therefore the observation of PL enhancement. Low-temperature PL and time-resolved PL were also measured and presented in Figure S13–S15 (Supporting Information).

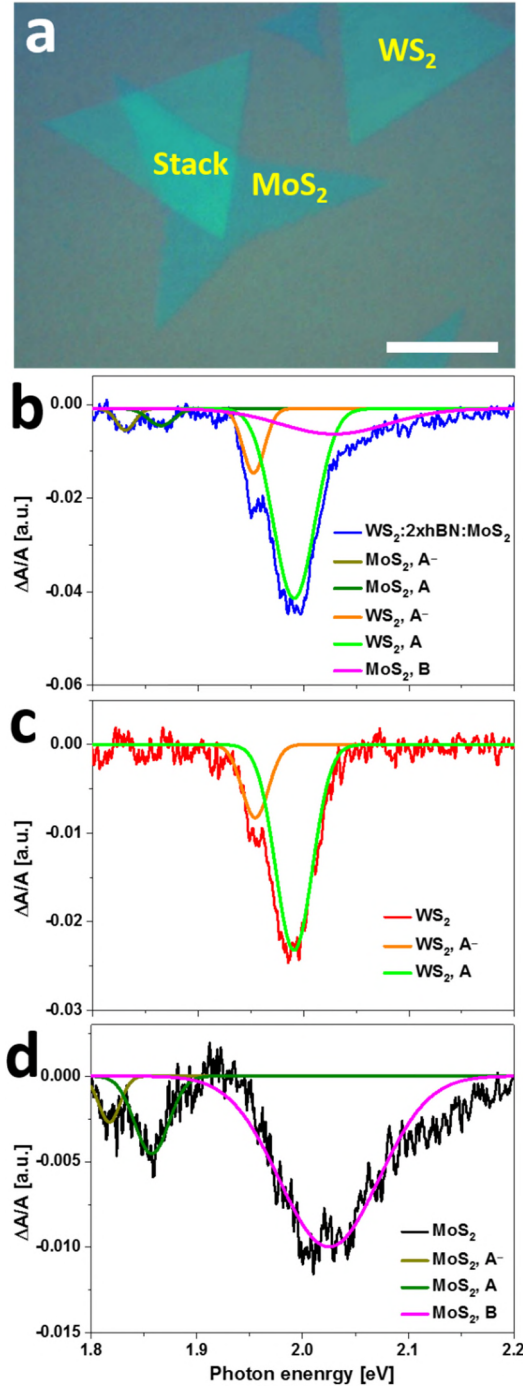


Figure 8. Femtosecond transient absorption spectroscopy. a) Optical microscope image with the regions marked for measurements. Scale bar: 50 μm . Gaussian-fitted TA spectra of b) $\text{WS}_2\text{:}2\times\text{hBN}\text{:MoS}_2$ VLH, c) WS_2 monolayer, and d) MoS_2 monolayer. The data were recorded at 1.5 ps pump-probe delay under a femtosecond pulse laser (~ 120 fs, 1 kHz) at 400 nm (3.10 eV) with a fluence of $\sim 1500 \mu\text{J cm}^{-2}$.

Table 1. Peak intensity with corresponding photon energy based on the Gaussian-fitted spectra in Figure 8.

Material	Peak intensity [a.u.] (Photon energy [eV])				
	$\text{MoS}_2 \text{ A}^-$	$\text{MoS}_2 \text{ A}$	$\text{WS}_2 \text{ A}^-$	$\text{WS}_2 \text{ A}$	$\text{MoS}_2 \text{ B}$
Stack	-0.005 (1.83)	-0.004 (1.86)	-0.014 (1.95)	-0.041 (1.99)	-0.005 (2.03)

WS ₂			−0.008 (1.95)	−0.023 (1.99)	
MoS ₂	−0.003 (1.82)	−0.005 (1.86)			−0.010 (2.03)

3. Conclusions

In summary, the results presented in this work show that the interlayer interactions between WS₂ and MoS₂ in vertically stacked heterostructures are highly dependent upon both the input excitation power and the separation distance. When no hBN spacer is used, only strong PL quenching is observed in our measurements and for 1 and 2 layers of hBN, we see that increasing laser power can switch the PL response from quenching to enhancement. Increasing excitation power has a direct effect on the exciton generation rate, with higher laser power exciting more excitons per unit area per second in the VLH stacks. Förster excitonic energy transfer involves dipole-dipole interactions and our results indicate that increasing the density of excitons in the VLH leads to stronger interactions between the two TMD materials. The efficiency of Förster energy transfer can also be improved by suppressing non-radiative decay channels at lower temperatures, which enables the observation of much larger PL enhancement. Förster energy transfer typically requires resonant energy levels and one explanation is the transfer of B exciton from MoS₂ to A exciton state in WS₂. The strong spectral overlap between the MoS₂ B exciton and WS₂ A exciton position makes it difficult to separate these from one another, but confirms their resonant condition. More investigation is needed to reveal the detailed mechanism of this higher level Förster energy transfer, while is the subject of future work beyond what we report here.

4. Experimental Section

Materials: The monolayer WS₂ domains were grown by hydrogen-free chemical vapour deposition in atmospheric pressure with the reactants of tungsten trioxide (WO₃, powder, 99.9%, Sigma-Aldrich) and sulphur (S, powder, ≥99.5%, Sigma-Aldrich).³⁸ To avoid solid-

phase reactions between the two precursors, 200 mg WO_3 was firstly placed in a smaller quartz tube, which was then mounted into a larger quartz tube with 400 mg sulphur pre-loaded. A 300 nm SiO_2/Si substrate was positioned 9.5 cm downstream of the WO_3 . Argon was introduced with a flow rate of 250 sccm to transport the precursor vapors onto the substrate surface. Two furnaces were used for independent temperature control. The sulphur reached its target temperature of 180 °C 10 min before WO_3 was finally heated to 1070 °C (ramp rate: $\sim 30\text{ }^\circ\text{C min}^{-1}$ for sulphur, and $\sim 40\text{ }^\circ\text{C min}^{-1}$ for WO_3). The reaction then lasted for 3 min, after which the sample was rapidly cooled down to room temperature.

A similar strategy was adopted to produce monolayer MoS_2 , utilizing the same set of double-walled quartz tubes.^[39] Molybdenum trioxide (MoO_3 , powder, $\geq 99.5\%$, Sigma-Aldrich) and sulphur (S, powder, $\geq 99.5\%$, Sigma-Aldrich) are employed as the precursors. The MoO_3 (inner tube, 20 mg) and S (outer tube, 300 mg) were ramped to ~ 180 and ~ 300 °C, respectively, while the 300 nm SiO_2/Si substrate located downstream was kept at ~ 800 °C to form MoS_2 monolayers. Note that the sulphur vapour was flushed through the system for 10 min before heating up the MoO_3 . Once the target temperature was reached, the MoS_2 nucleates firstly with 150 sccm argon flow for 17 min, and then the flow rate was reduced to 10 sccm for a 23-min growth. Finally, the reaction was ceased with a fast cooling process.

The hBN films were also synthesized via CVD method on copper foil (25 μm , Alfa Aesar), using ammonia borane (H_3NBH_3 , powder, $\geq 97\%$, Sigma-Aldrich) as the precursor. In order to smoothen the reaction surface, the substrate was first annealed at 1000 °C for 1 h. Then the precursor (7 mg) was evaporated at ~ 130 °C, and carried by 120 sccm hydrogen. The growth was carried out at 1050 °C in another furnace. The growth time was precisely controlled to obtain continuous films with different thicknesses (15 min for monolayer hBN and 17 min for bilayer hBN). The sample was cooled rapidly after the growth.

Fabrication of VLHs: The as-grown sample was first spin-coated with a thin poly(methyl

methacrylate) (PMMA) supporting layer at 4500 rpm for 60 s and then cured at 180 °C for 90 s. The 300 nm SiO₂/Si substrate was detached from the TMD layer by floating the sample on a 1 M potassium hydroxide (KOH) aqueous solution, whereas the copper substrate was dissolved by 0.2 M ammonium persulfate ((NH₄)₂S₂O₈, APS) aqueous solution. This process can be accelerated by a water bath at ~50 °C. The isolated film was subsequently rinsed in deionized (DI) water three times for 1 h each. After that, a piece of clean cover glass was submerged into the DI water to fish the film. Then a few drops of isopropanol (IPA) were applied onto the cover glass to expel the residual water before the film slid slowly onto the designated substrate.^[35] After being air-dried overnight, the sample was baked at 150 °C for 30 min to enhance the interface adhesion. Finally, the PMMA coating was removed in acetone for 3 h. The layer-by-layer heterostructures were assembled by repeating this transfer procedure.

Characterization: Optical microscopy and scanning electron microscopy (Hitachi-4300, 3.0 kV accelerating voltage) were used to image the samples. The thickness of hBN films was examined with an atomic force microscope (Asylum Research MFP-3D). Typical scans were performed across the film edges in AC mode utilizing a silicon AC160TS cantilever (Olympus, spring constant of ~42 N m⁻¹ and resonant frequency of ~300 kHz). Raman and photoluminescence (PL) spectroscopy were conducted under an imaging confocal Raman microscope (JY Horiba LabRAM ARAMIS). A 532 nm (2.33 eV) diode laser was used for the room-temperature PL. The incident laser power was changed by adjusting different neutral density filters. Broadband transient absorption was measured with a 300 nW femtosecond pulse laser (~120 fs, 1 kHz) at 400 nm (3.10 eV). The photoinduced changes in the absorption spectrum (ΔA) was probed by a laser-generated supercontinuum light after controlled time delays. The low-temperature PL and time-resolved PL were tested by time-correlated single photon counting (TCSPC) under a 20 μ W, 405 nm (3.06 eV) diode laser

(Becker & Hickl GmbH BDL-405-SMN). The emitted photons were detected by ANDOR SR-500i-B1-R spectrometer, and analyzed by a TCSPC board (Becker & Hickl SPC-100). A liquid nitrogen cooling system was equipped to achieve cryogenic temperatures. The spot size of $\sim 1\ \mu\text{m}$ was kept constant for different lasers, except in the transient absorption measurements where the pump light has a spot size of $\sim 6\ \mu\text{m}$ and a fluence of $\sim 1500\ \mu\text{J cm}^{-2}$. The acquisition time for the PL spectrum and each point in PL mapping were 1 s and 0.1 s, respectively.

Image Processing: The atomic models were generated using Accelrys Discovery Studio Visualizer. Each point in the PL maps corresponds to a PL spectrum from that local position. The integration ranges of PL intensities are 1.84–2.09 eV for $\text{WS}_2\text{:hBN:MoS}_2$ VLHs, and 1.80–2.05 eV for $\text{MoS}_2\text{:hBN:WS}_2$ VLHs, given the red-shifted PL peak position of strained WS_2 monolayers. The highest integration values were normalized to the same scale for all the VLHs studied in this work.

Supporting Information

Supporting Information is available from the Wiley Online Library or from the author.

Acknowledgments

JHW thanks the Royal Society for support.

References

- [1] L. Britnell, R. V. Gorbachev, R. Jalil, B. D. Belle, F. Schedin, A. Mishchenko, T. Georgiou, M. I. Katsnelson, L. Eaves, S. V. Morozov, N. M. R. Peres, J. Leist, A. K. Geim, K. S. Novoselov, L. A. Ponomarenko, *Science* **2012**, 335, 947.
- [2] X. Cui, G.-H. Lee, Y. D. Kim, G. Arefe, P. Y. Huang, C.-H. Lee, D. A. Chenet, X. Zhang, L. Wang, F. Ye, F. Pizzocchero, B. S. Jessen, K. Watanabe, T. Taniguchi, D. A. Muller, T. Low, P. Kim, J. Hone, *Nat. Nanotechnol.* **2015**, 10, 534.
- [3] G.-H. Lee, Y.-J. Yu, X. Cui, N. Petrone, C.-H. Lee, M. S. Choi, D.-Y. Lee, C. Lee, W. J.

- Yoo, K. Watanabe, T. Taniguchi, C. Nuckolls, P. Kim, J Hone, *ACS Nano* **2013**, 7, 7931.
- [4] T. Georgiou, R. Jalil, B. D. Belle, L. Britnell, R. V. Gorbachev, S. V. Morozov, Y.-J. Kim, A. Gholinia, S. J. Haigh, O. Makarovskiy, L. Eaves, L. A. Ponomarenko, A. K. Geim, K. S. Novoselov, A. Mishchenko, *Nat. Nanotechnol.* **2013**, 8, 100.
- [5] H. Tan, Y. Fan, Y. Rong, B. Porter, C. S. Lau, Y. Zhou, Z. He, S. Wang, H. Bhaskaran, J. H. Warner, *ACS Appl. Mater. Interfaces* **2016**, 8, 1644.
- [6] T. Roy, M. Tosun, X. Cao, H. Fang, D.-H. Lien, P. Zhao, Y.-Z. Chen, Y.-L. Chueh, J. Guo, A. Javey, *ACS Nano* **2015**, 9, 2071.
- [7] F. Withers, T. H. Bointon, D. C. Hudson, M. F. Craciun, S. Russo, *Sci. Rep.* **2014**, 4, 4967.
- [8] C. Gong, H. Zhang, W. Wang, L. Colombo, R. M. Wallace, K. Cho, *Appl. Phys. Lett.* **2013**, 103, 053513.
- [9] O. Lopez-Sanchez, E. Alarcon Llado, V. Koman, A. Fontcuberta i Morral, A. Radenovic, A. Kis, *ACS Nano* **2014**, 8, 3042.
- [10] K. F. Mak, C. Lee, J. Hone, J. Shan, T. F. Heinz, *Phys. Rev. Lett.* **2010**, 105, 136805.
- [11] S. Tongay, J. Zhou, C. Ataca, K. Lo, T. S. Matthews, J. Li, J. C. Grossman, J. Wu, *Nano Lett.* **2012**, 12, 5576.
- [12] W. Zhao, Z. Ghorannevis, L. Chu, M. Toh, C. Kloc, P.-H. Tan, G. Eda, *ACS Nano* **2013**, 7, 791.
- [13] C. Cong, J. Shang, X. Wu, B. Cao, N. Peimyoo, C. Qiu, L. Sun, T. Yu, *Adv. Opt. Mater.* **2014**, 2, 131.
- [14] A. Splendiani, L. Sun, Y. Zhang, T. Li, J. Kim, C.-Y. Chim, G. Galli, F. Wang, *Nano Lett.* **2010**, 10, 1271.
- [15] A. Ramasubramaniam, *Phys. Rev. B* **2012**, 86, 115409.
- [16] H. Sahin, S. Tongay, S. Horzum, W. Fan, J. Zhou, J. Li, J. Wu, F. M. Peeters, *Phys. Rev.*

B **2013**, 87, 165409.

- [17] Y. He, Y. Yang, Z. Zhang, Y. Gong, W. Zhou, Z. Hu, G. Ye, X. Zhang, E. Bianco, S. Lei, Z. Jin, X. Zou, Y. Yang, Y. Zhang, E. Xie, J. Lou, B. Yakobson, R. Vajtai, B. Li, P. Ajayan, *Nano Lett.* **2016**, 16, 3314.
- [18] H.-P. Komsa, A. V. Krasheninnikov, *Phys. Rev. B* **2013**, 88, 085318.
- [19] K. Kośmider, J. Fernández-Rossier, *Phys. Rev. B* **2013**, 87, 075451.
- [20] X. Hong, J. Kim, S.-F. Shi, Y. Zhang, C. Jin, Y. Sun, S. Tongay, J. Wu, Y. Zhang, F. Wang, *Nat. Nanotechnol.* **2014**, 9, 682.
- [21] A. F. Rigosi, H. M. Hill, Y. Li, A. Chernikov, T. F. Heinz, *Nano Lett.* **2015**, 15, 5033.
- [22] H. Fang, C. Battaglia, C. Carraro, S. Nemsak, B. Ozdol, J. S. Kang, H. A. Bechtel, S. B. Desai, F. Kronast, A. A. Unal, G. Conti, C. Conlon, G. K. Palsson, M. C. Martin, A. M. Minor, C. S. Fadley, E. Yablonovitch, R. Maboudian, A. Javey, *Proc. Natl. Acad. Sci.* **2014**, 111, 6198.
- [23] C. H. Lui, Z. Ye, C. Ji, K.-C. Chiu, C.-T. Chou, T. I. Andersen, C. Means-Shively, H. Anderson, J.-M. Wu, T. Kidd, Y.-H. Lee, R. He, *Phys. Rev. B* **2015**, 91, 165403.
- [24] M. S. Kim, C. Seo, H. Kim, J. Lee, D. H. Luong, J.-H. Park, G. H. Han, J. Kim, *ACS Nano* **2016**, 10, 6211.
- [25] Y. Gong, J. Lin, X. Wang, G. Shi, S. Lei, Z. Lin, X. Zou, G. Ye, R. Vajtai, B. I. Yakobson, H. Terrones, M. Terrones, B. K. Tay, J. Lou, S. T. Pantelides, Z. Liu, W. Zhou, P. M. Ajayan, *Nat. Mater.* **2014**, 13, 1135.
- [26] H. Terrones, F. López-Urías, M. Terrones, *Sci. Rep.* **2013**, 3, 1549.
- [27] M. M. Furchi, A. Pospischil, F. Libisch, J. Burgdörfer, T. Mueller, *Nano Lett.* **2014**, 14, 4785.
- [28] S. Tongay, W. Fan, J. Kang, J. Park, U. Koldemir, J. Suh, D. S. Narang, K. Liu, J. Ji, J. Li, R. Sinclair, J. Wu, *Nano Lett.* **2014**, 14, 3185.

- [29] J. Kang, J. Li, S.-S. Li, J.-B. Xia, L.-W. Wang, *Nano Lett.* **2013**, *13*, 5485.
- [30] A. Olaya-Castro, G. D. Scholes, *Int. Rev. Phys. Chem.* **2011**, *30*, 49.
- [31] Z. He, W. Xu, Y. Zhou, X. Wang, Y. Sheng, Y. Rong, S. Guo, J. Zhang, J. M. Smith, J. H. Warner, *ACS Nano* **2016**, *10*, 2176.
- [32] J. Shang, X. Shen, C. Cong, N. Peimyoo, B. Cao, M. Eginligil, T. Yu, *ACS Nano* **2015**, *9*, 647.
- [33] T. Schmidt, K. Lischka, W. Zulehner, *Phys. Rev. B* **1992**, *45*, 8989.
- [34] T. Kato, T. Kaneko, *ACS Nano* **2014**, *8*, 12777.
- [35] Y. Sheng, W. Xu, X. Wang, Z. He, Y. Rong, J. H. Warner, *Nanoscale* **2016**, *8*, 2639.
- [36] A. Berkdemir, H. R. Gutiérrez, A. R. Botello-Méndez, N. Perea-López, A. L. Elías, C.-I. Chia, B. Wang, V. H. Crespi, F. López-Urías, J.-C. Charlier, H. Terrones, M. Terrones, *Sci. Rep.* **2013**, *3*, 1755.
- [37] C. Lee, H. Yan, L. E. Brus, T. F. Heinz, J. Hone, S. Ryu, *ACS Nano* **2010**, *4*, 2695.
- [38] Y. Rong, Y. Fan, A. L. Koh, A. W. Robertson, K. He, S. Wang, H. Tan, R. Sinclair, J. H. Warner, *Nanoscale* **2014**, *6*, 12096.
- [39] S. Wang, Y. Rong, Y. Fan, M. Pacios, H. Bhaskaran, K. He, J. H. Warner, *Chem. Mater.* **2014**, *26*, 6371.
- [40] B. Bansal, A. Kadir, A. Bhattacharya, V. V. Moshchalkov, *Appl. Phys. Lett.* **2008**, *93*, 021113.
- [41] A. V. Stier, K. M. McCreary, B. T. Jonker, J. Kono, S. A. Crooker, *Nat. Commun.* **2016**, *7*, 10643.
- [42] D. Kozawa, A. Carvalho, I. Verzhbitskiy, F. Giustiniano, Y. Miyauchi, S. Mouri, A. H. Castro Neto, K. Matsuda, G. Eda, *Nano Lett.* **2016**, *16*, 4087.
- [43] Y. Wang, C. Cong, W. Yang, J. Shang, N. Peimyoo, Y. Chen, J. Kang, J. Wang, W. Huang, T. Yu, *Nano Res.* **2015**, *8*, 2562.

- [44] E. Scalise, M. Houssa, G. Pourtois, V. Afanas'ev, A. Stesmans, *Nano Res.* **2012**, 5, 43.
- [45] N. Peimyoo, J. Shang, C. Cong, X. Shen, X. Wu, E. K. L. Yeow, T. Yu, *ACS Nano* **2013**, 7, 10985.